Geomorphology 462 (2024) 109332

Contents lists available at ScienceDirect

Geomorphology

journal homepage: www.journals.elsevier.com/geomorphology

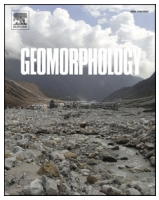

Possibilities and limitations of cave detection with ERT

Barbara Funk [a,b,*], Adrian Flores-Orozco [a], Matthias Steiner [a]

[a] Research Division Geophysics, TU-Wien, Wiedner Hauptstraße 8-10, Vienna, 1040 Vienna, Austria
[b] Karst and Cave Group, Natural History Museum, Museumsplatz 1/10/4, Vienna, 1070 Vienna, Austria

ARTICLE INFO

Keywords:
Speleology
Case study
Forststraßeneinbruch
Karst
ERT
Geomorphology

ABSTRACT

About 15 % of the global ice-free continental surface is characterized by the presence of karstifiable carbonate rock. In Austria, about 20 % of the surface area consists of water-soluble rocks such as limestone or dolomite. Karstification may result in the formation of various cavities with varying size and distribution. Karst massifs are highly complex systems in which the water moves along different geological discontinuities that range in a broad spatial scale, from intragranular cracks (in the micro- to centimeter range) to fractures and cave systems, which can extend over kilometers. Electrical resistivity tomography (ERT) is widely used for cave detection, yet associated limitations have not been addressed so far. This study investigates subsurface conditions favoring the detection of cavities with ERT as well as the geological settings limiting the method. In a first step, we use a numerical study to evaluate the ability of the inversion method to recover the geometry of well-known resistivity anomalies, by varying the resistivity values of the host rock. Synthetic data is used to understand the contrasts required between the anomaly and the host rock. In a second step, we present extensive ERT data collected to delineate the geometry of the "Forststraß eneinbruch" cavity. This area is located near Lunz am See in the Northern Calcareous Alps and was first mentioned in December 2016 due to a sinkhole formed on a forest road. The geometry of the accessible parts of the cave was recorded using a speleological survey and could be used to evaluate the field results. Moreover, ERT result can be used to detect other cavities not found during the speleological survey. By using the speleological survey data we could create realistic models of the subsurface, from which synthetic data were derived to understand the ability of the inversion to retrieve a well-known model.

The ERT images show in general a good agreement with the known geometry of the cave and could be validated through the synthetic models and the further available information. However, the size of the anomalies point out to the presence of further caves. The synthetic results revealed that the resistive anomaly related to the cave is better resolved in presence of a resistive host rock. While decreasing the resistivity of the host rock leads to a decrease also in the sensitivity of the method to sense the cave, likely due to the ability of the current to easily move around the resistive anomaly.

1. Introduction

According to Goldscheider et al. (2020) about 15 % of the global ice-free continental surface is characterized by the presence of karstifiable carbonate rock. In Austria, about 20 % of the surface area consists of water-soluble rocks such as limestone or dolomite (Spötl et al., 2016). Karstification may result in the formation of various cavities with varying size and distribution. Karst massifs are highly complex systems in which water moves along various geological discontinuities that range in spatial scale from intragranular cracks (micro- to centimeter-scale) to fractures and cave systems that can extend for kilometers (De Waele and Gutiérrez, 2022). Knowledge about the position and geometry of near-surface caves is critical to prevent damages to infrastructure due to the collapse of the caves, which may also pose a threat to human life [e.g. (De Waele and Gutiérrez, 2022; Park et al., 2024; Puzzilli et al., 2024)]. Since such cavities often have no connection to the surface (accessible to humans), their geometry cannot always be determined through speleological surveys.

Geophysical methods have been proven to be well-suited methods to gain non-destructive quasi-continuous information about subsurface structures. In karst systems this may be of particular interest where near-surface cavities are suspected, but not accessible [e.g. (Chalikakis et al.,

* Corresponding author at: Research Division Geophysics, TU-Wien, Wiedner Hauptstraße 8-10, Vienna, 1040 Vienna, Austria.
E-mail address: barbara.funk@geo.tuwien.ac.at (B. Funk).

https://doi.org/10.1016/j.geomorph.2024.109332
Received 19 April 2024; Received in revised form 7 July 2024; Accepted 8 July 2024
Available online 14 July 2024

2011; Verdet et al., 2020; Martínez-Moreno et al., 2014; Amanatidou et al., 2022; Ba et al., 2020; Yue et al., 2020; Pasierb, 2022)]. Considering the contrasts in the resistivity of typical subsurface materials in karstic systems (e.g., limestone, sediment, clay, air), ERT is a widely used geophysical method for the delineation of underground cavities and karstic phenomenons [e.g. (Khaldaoui et al., 2020; Valois et al., 2011; Zhang et al., 2019; Gómez-Ortiz and Martín-Crespo, 2012; Artugyan et al., 2020; Tao et al., 2022)]. Typical geological materials of the host rocks (e.g., limestones) are related, depending on the saturation, to modest to high electrical resistivity values; whereas karstic features such as caves and fractures can be linked to (i) an increase in the electrical resistivity values due to conduits filled with air [e.g. (Carriére et al., 2013; Su et al., 2021)]; or to (ii) a decrease in the electrical resistivity, associated to conduits filled with clay, or wet sediments [e.g. (Martel et al., 2018; Cheng et al., 2019)].

In this study we aim at gaining a better understanding on the imaging capabilities of the ERT method based on a carefully designed numerical study. In particular, we investigate the influence of the resistivity contrast in the subsurface by using (i) a resistive anomaly associated to air filling of the open space, or (ii) when the walls of the cave are conductive associated to walls covered with wet clayey grains transported during the infiltration of surface water. Additionally we reviewed the influence of a soil layer on the surface above the cave. We then apply the approach demonstrated by the numerical study to field data, using measurements above the Forststraß eneinbruch a cave located in Austria (near Lunz am See). Available ground truth data allow for interpretation of the ERT results leading to the delineation of unknown cave parts.

2. Materials and methods

2.1. The resistivity properties of rock

The subsurface resistivity (ρ), or its inverse the electrical conductivity ($\sigma = 1/\rho$), is controlled by three conduction mechanisms [e.g. (Niggli, 1948)]: (1) Matrix conduction, through the solid part of the rock, which is negligible in media without electrical conductors (i.e., metals), as expected for karstic regions.

(2) Electrolytic conduction (σ_f) refers to the migration of the electric charge through the water present in pores and cracks (i.e., ions dissolved in the electrolyte filling of the pore-space). Therefore, the volume, diameter and interconnectivity of the pore spaces between individual minerals (porosity), water saturation and the concentration, charge and mobility of ions are relevant to the electrical conductivity of the entire rock body.

(3) Surface conductivity refers to the migration of charges (i.e., ions) along the electrical double layer (EDL) formed at the gain-fluid interface. Hence, in the absence of electronic conductors (i.e., metals) it is controlled by the contribution of both surface and electrolytic conduction, with the former being controlled by the porosity, saturation of the pore-space and the salinity of the electrolytic; while the latter is controlled by the surface area and surface charge of grains. Archie's Law (Archie, 1942) has to be extended then by the surface conductivity (σ_s):

$$\sigma = \Phi^m \sigma_f S^n + \sigma_s \qquad [\ S/m], \tag{1}$$

where Φ is the porosity, S the saturation and m and n are fitting parameters of Archie's law [e.g. (Waxman and Smits, 1968; Revil and Glover, 1998)].

2.2. The ERT method

The ERT is an electrical method based on the injection of DC-current through a pair of electrodes (current electrodes) and measure of the resulting voltage in another pair (potential electrodes). From the known injected current (I) and the measured voltage (U), the resistance (R) can be calculated (R = U / I). In ERT, tens of electrodes are used to collect a hundreds of 4-electrode measurements, which can be used to resolve variations in the electrical resistivity of the subsurface through the inversion of the data (Binley and Kemna, 2005). For the inversion of the data we used CRTomo (Kemna, 2000). This iterative smoothness-constraint inversion algorithm allows the inversion of the data by specifying a confidence level given by the data error. CRTomo uses a linear relationship between the measured values (R) and their errors (s_R):

$$s_R = a + bR, \tag{2}$$

where a is the absolute error, relevant for low resistance values and b is a relative error (in percent), important for higher resistance values (LaBrecque et al., 1996). The exact distribution and dispersion of these random errors are not known. They can be estimated using normal and reciprocal, where the current and potential electrodes are changed [e.g. (LaBrecque et al., 1996; Flores Orozco et al., 2012; Flores Orozco et al., 2018)]. In CRTomo, the inversion stops when the modeled resistances are equal to the measured resistances weighted by the associated error parameter, i.e., when the error-weighted RMS (root-mean-square error) is equal to one. Further details can be found in Kemna (2000).

Electrical images show spatially variable image resolution [e.g. (Oldenburg and Li, 1999; Friedel, 2003; Binley and Kemna, 2005)], which should be taken into account when interpreting the images. Several studies have shown that an analysis of sensitivity provides valuable insight into the resolution problem of the ERT results (Kemna et al., 2002; Nguyen et al., 2009; Weigand et al., 2017). Here, sensitivity indicates how a local change in electrical conductivity affects a single measurement. A superposition of the individual sensitivities, the so-called cumulative sensitivity (Kemna, 2000), shows the coverage of the different region, whereas poorly covered regions normally also lead to poor resolution. Therefore, such cumulative sensitivity images can be used as a proxy for the resolution of the images. In this study, we take this into account by blanking model parameters in the imaging results with a cumulated sensitivity 2 orders of magnitude smaller than the largest cumulated sensitivities [e.g. (Weigand et al., 2017)]. Such approach has been largely investigated in other studies [e.g. (Flores Orozco et al., 2013)].

2.3. Study area, geology of the site and speleological data

The study area, the Schöfftaler Wald 5 km southwest of Lunz am See, is characterized by a high density of caves, most of which are developed in the Opponitzer Limestone (Bauer et al., 1988). The Forststraß eneinbruch was discovered in December 2016 (Fig. 1), because a sinkhole formed on a forest road. The sinkhole was formed in the unconsolidated rubble and soil material, which reaches the bedrock at a depth of ca. 2 m below ground surface (bgs). The rest of the cave is formed in Opponitzer limestone, stays mostly narrow and shows sticky layers of fine sediment. Speleologist surveys between 2016 and 2018 revealed that the Forststraßeneinbruch cave has a length of 147 m and a depth of 24 m (unpublished report in the cadastre of the Landesverein für Höhlenkunde in Wien und NÖ). For the speleological surveys a distance meter (Leica Disto) was used, which in addition to a laser distance measurement also provides a compass and an inclinometer. With the help of this device it is possible to lay a traverse through the cave, consisting of distance, azimut and inclination measurements, which can also be converted to X,Y,Z coordinates. Since such a traverse is just a line and does therefore not represent the geometry of a cave, speleologists additionally draw a ground plan and a longitudinal section (Fig. 2). Therefore additional measurements to the walls (splay shots) were recorded during the on-site survey. By using all this information we know the shape, size and depth of the cave in a local, north-facing coordinate system with the origin at the cave entrance.

Fig. 1. Picture of the provisionally covered entrance of Forststraßeneinbruch, also visible the ERT instrument and the cables.

2.4. Geophysical data collection and processing

The ERT survey was designed to cover most of the surface above the known area of the Forstraß eneinbruch cave using 2D lines. The use of 3D measurements helps to improve the resolution of the resistivity model within the lines [e.g. (Moser et al., 2023)], yet due to the dense vegetation, the conduction of 2D lines is more effective. Hence, ERT was collected along seven profiles (Fig. 2a), each with 72 electrodes and an electrode spacing of 1 m, where the parallel profiles **P3** to **P7** had a distance of about 3 m between them. While the electrodes were mostly located on forest soil resulting in low contact resistances ($< 10\ \Omega$) a few electrodes were placed on forest roads resulting in higher contact resistances (up to 230 Ω). For the measurements presented here we used a Syscal device (Syscal Pro Switch 72, IRIS instruments) with ten channels. For each profile we recorded a total of 2068 quadrupoles in a dipole-dipole configuration with different dipole length (i.e., skips). In particular data were collected with skip-0, −1 up to skip-11 (i.e., from 1 to 12 times the electrode separation) and all levels (from the minimal to the maximum possible separation between current and potential dipoles). As reciprocal readings were not feasible due to limited time for the survey, outliers were identified by means of the analysis of histograms [e.g. (Flores Orozco et al., 2018)], which represent the distribution of the recorded data. In a first step all negative apparent resistivities are removed. The examination of the histograms of all seven profiles has revealed a common threshold value of $10^5\ \Omega m$ for the maximum accepted apparent resistivity, with all readings exceeding this considered as outliers. The best results (resulting in an RMS equal to 1) for all profiles were achieved with the following error values:

Resistance errors: a = 5 %, b = 0.01.

The coordinates of the electrodes of all profiles were recorded using a tachymeter (Leica TPS 1100) and subsequently transformed to the coordinate system of the cave survey. Based on the profiles and cave survey coordinates, as well as the ground plan and the longitudinal section we created maps of the subsurface below all seven profiles that can be compared with the results of the measurements. Furthermore these maps were also used to create electrical models of the subsurface for the validation of the ERT results.

2.5. Numerical experiments to investigate the resolution capabilities by changing the resistivity contrasts between the cave, its filling and the background

To investigate the limitations of the ERT-based cave detection, we conducted studies on synthetic models assuming 72 electrodes with 1 m spacing and the measuring protocol used on the field survey. The model also includes an anomaly with a diameter of 5 m at a depth of 5 m ($10^6\ \Omega$m) and a surrounding background (500, 1000, 5000 Ωm). For our investigations we considered the following model parametrization: (**m1**) a resistive background encompassing a high resistivity anomaly, (**m2**) a thin shallow layer simulating conductive soil (100 Ωm) on top of a resistive background encompassing a high resistivity anomaly, (**m3**) a resistive background encompassing a high resistivity anomaly featuring a thin conductive layer (100 Ωm) at the bottom (emulating sediments accumulating on wet cave floors or in fractures and other surface roughness), and three more models (**m4**, **m5** and **m6**) from the combination of **m2** and **m3**. For each parametrization we forward modeled the electrical response of the different background resistivity values. These measurements were conducted to understand the parameters controlling the resolution and depth of investigation in our ERT survey. A summary of all the models created is shown in Table 1.

2.6. Numerical models to evaluate the resolution of field data to recover the known geometry of the Forststraß eneinbruch cave

To support the interpretation of the field data imaging results we built synthetic subsurface models considering the known topography of the profiles above the Forststraß eneinbruch. Here an air-filled cavity ($\rho = 10^6\ \Omega$m) was assumed at the actual position and geometry of the Forststraß eneinbruch, obtained from the speleological survey data and the cave plan. For the bedrock we assume a resistivity value of 5000 Ωm and for the soil layer 200 Ωm (Table 1). For forward modeling the synthetic data we considered the same electrode configuration and settings as in the field data.

From the resistivity models we derived synthetic data using the finite-element modeling code CRMod (Kemna, 2000). Further details on

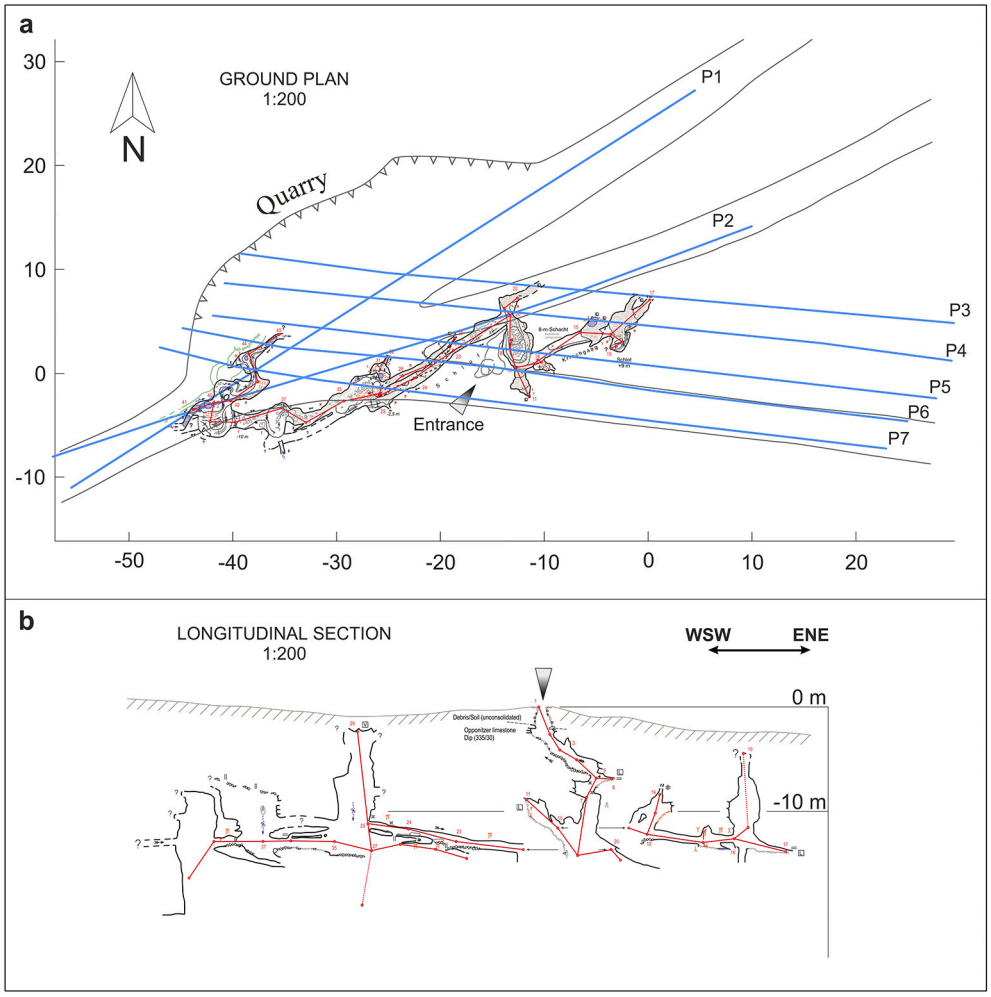

Fig. 2. Shown are the ground plan (**a**) and the longitudinal section (**b**) of the Forststraßeneinbruch. Given are the traverse (red line), the survey points (red dots with red numbers) and a graphical representation of the cave chambers, drawn on site. In the ground plan (**a**) also a schematic map with the forest roads and the quarry and the seven profiles (blue lines) are shown.

Table 1
Summary of all models investigated. Given are the resistivity values for the background, the cave and the soil layer at the surface (soil) and in the cave (clay).

Model	Figure	Background [Ωm]	Cave [Ωm]	Soil [Ωm]	Clay [Ωm]
m1	3 (d, g, k)	500, 1000, 5000	10^6	–	–
m2	3 (e, h, l)	500, 1000, 5000	10^6	100	–
m3	3 (f, i, m)	500, 1000, 5000	10^6	–	100
m4	4 (r, u, x)	500, 1000, 5000	10^6	100	100
m5	4 (s, v, y)	500, 1000, 5000	10^6	100	200
m6	4 (t, w, z)	500, 1000, 5000	10^6	200	100
P1-P7	5 (c, f, i, m, p, t, w)	5000	10^6	200	–

the implementation can be found in Kemna (2000). The data noise always present in the measurements is generated here by adding random noise characterized by a random error of ±3 % for the models **m1** to **m6** and ±5 % for the models of **P1** to **P7**.

3. Results and discussion

3.1. Synthetic study - the influence of a soil layer and clay adhered on cavity walls

Fig. 3 presents the resistivity model after the inversion of the forward response. For model **m1** (Fig. 3a) one can see an increase in the reconstruction capabilities with increasing resistivity of the background (Fig. 3d, g, k). For the lower resistivity values of the background (ρ = 500, 1000 Ωm, Fig. 3d, g) the electrical resistivity images fail to detect the position of the cave, which can be explained by the fact that rocks with lower resistivity conduct the current better and thus can mask a cavity. In the case of model **m2** (Fig. 3b) it can be seen that a conductive soil layer reduces the depth of investigation (Fig. 3e, h, c), which also negatively affects the reconstruction capability of the method to resolve for the cave in terms of both geometry and resistivity value. The soil layer above the cave is only clearly visible in the inversion image with a soil resistivity of 5000 Ωm (Fig. 3l), while it is only indicated in Fig. 3h and not visible in Fig. 3e. Where it is visible, the thickness of the soil layer is overestimated. To investigate the influence of a soil layer, Fig. 4 shows, as an example, the sensitivities of the inversions of the models **m1** (Fig. 3k) and **m2** (Fig. 3l). In both cases the sensitivity of the near-surface layer (first 1–2 m) is approximately the same, while the model without a soil layer (Fig. 4a) shows a higher sensitivity even at greater depths, this decreases faster in the model with a soil layer (Fig. 4b). From

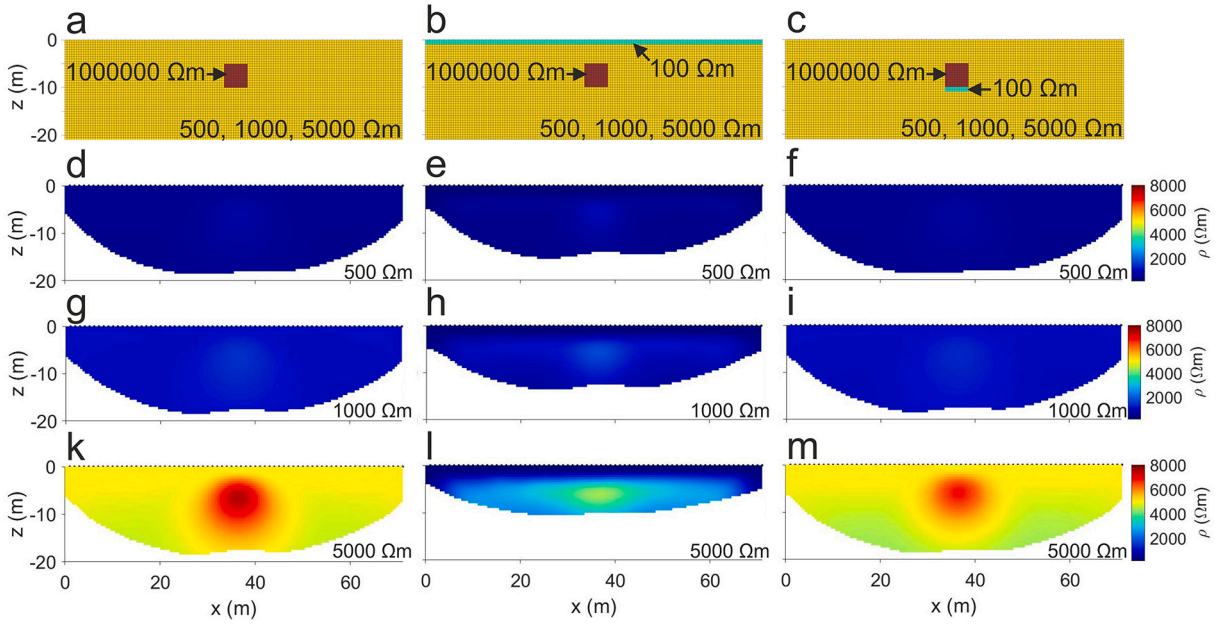

Fig. 3. Numerical and inversion models from the synthetic study. n - p: resistivity distribution; resistive anomaly (1000000 Ωm), conductive layer (100 Ωm) and surrounding bedrock (500, 1000, 5000 Ωm). d - m: the inversion results.

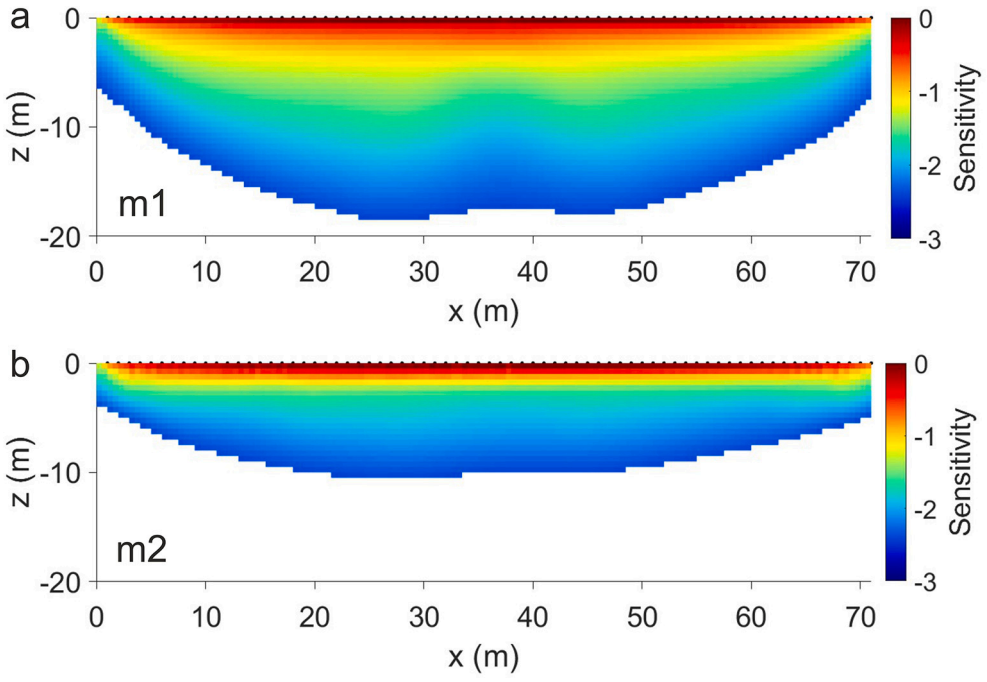

Fig. 4. Sensitivities of the inversions of the models **m1** (a) and **m2** (b) each for a background resistivity of 5000 Ωm.

this it can be concluded that most of the current flows through the well-conducting layer near the surface and only little reaches deeper layers. However, if there is no soil layer, the current reaches greater depths, which is reflected in a greater depth of investigation. Similar to the results for the model **m1** (Fig. 3d, g, k), the cavity is also not visible in the inversion images of the model **m3** (Fig. 3f, i) for a background with lower resistivity (500, 1000 Ωm). The resistivity image with a high resistivity background (Fig. 3m) performs better in terms of reconstructing the geometry and location of the cavity. Nevertheless, the geometry of the cave is not correctly reproduced, but overestimated compared to the real model (Fig. 3c). For models **m4** and **m5** (Fig. 5n, o) we added both a conductive layer on the surface (100 Ωm) and at the caves floor (100 Ωm for model **m4** (Fig. 5n) and 200 Ωm for model **m5** (Fig. 5o)). The inversion images of both models (Fig. 5r, u, x, s, v, y) show similar behavior and no difference to those resulting from model **m2** (Fig. 3b, e, h, l). Hence, the existence of a thin layer associated to sediments accumulated on the cave floor cannot counterbalance the negative effect of a conductive soil layer. In a last experiment, we repeated the modeling for a more resistive soil layer (200 Ωm) on the surface and a soil layer on the floor of the cave of 100 Ωm (model **m6**, Fig. 5p). The inversion image for a background resistivity of 5000 Ωm (Fig. 5,z) shows both the boundary between the soil on the surface and the background as well as the position of the cave. Hence, even a slightly less conductive soil layer (200 instead of 100 Ωm) is sufficient to

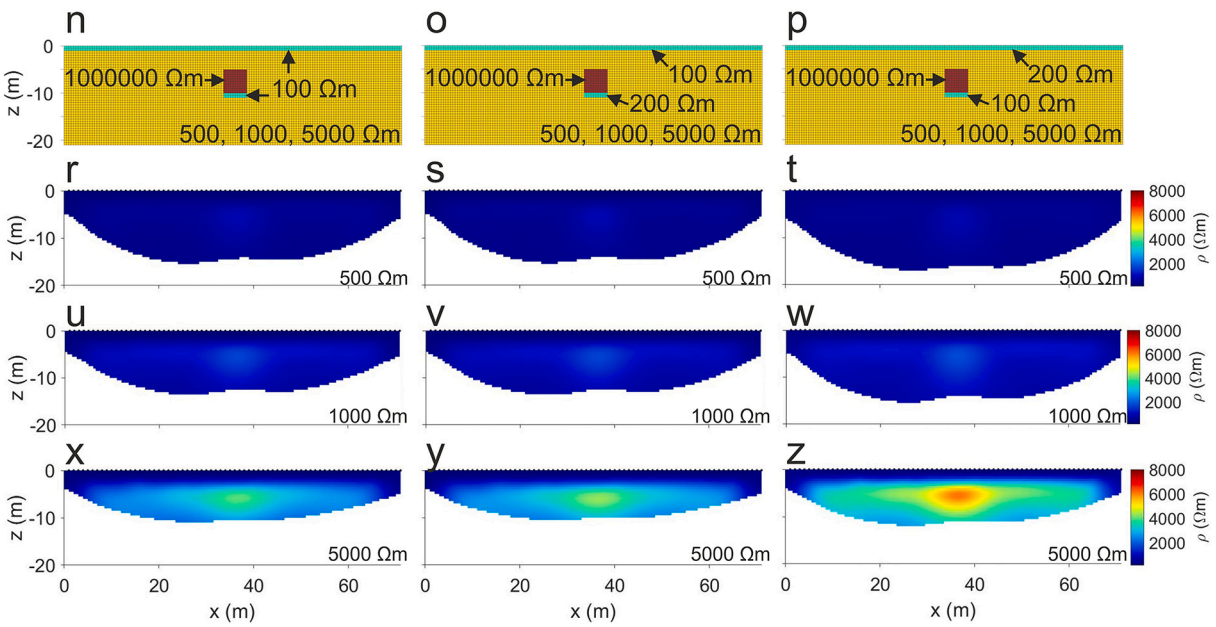

Fig. 5. Numerical and inversion models from the synthetic study. n - p: resistivity distribution; resistive anomaly (1000000 Ωm), conductive layer (100 Ωm) and surrounding bedrock (500, 1000, 5000 Ωm). r - z: the inversion results.

increase the sensitivity at depth and thus enable the detection of a cave.

3.2. *Field data results and the reconstruction capabilities through synthetic modeling*

Fig. 6 shows the inversion results for all seven profiles and their interpretation (first and second column in Fig. 6 respectively), including the known outlines of Forststraß eneinbruch as well as, the inversion results of the synthetic data obtained by the resistivity models generated assuming 5000 Ωm for the bedrock, a soil layer ($\rho = 200$ Ωm) and high resistivity values ($\rho = 10^6$ Ωm) at the position of the known geometry of the cave (last column in Fig. 6). The inversion results of this synthetic data allow us to evaluate whether the interpretation of the resistivity anomalies can be explained by the cave. Sensitivity analysis reveals that along all profiles the maximum depth of investigation is not deeper than 15 m, at which the sensitivity in the model parameters is at least 1000 times worse than the best resolved parameters next to the electrode positions, thus allowing for the delineation of the shallow cavities from the Forststraß eneinbruch. In general, all profiles reveal three main units: (i) low resistivity values (below 200 Ωm) which correspond to soil and sediments on the surface; (ii) intermediate to high resistivity values (between 500 and 6000 Ωm) which correspond to the bedrock, and (iii) high resistivity anomalies (> 7000 Ωm), which we interpret as caves.

In the resistivity image of **P1** (Fig. 6a) the boundary between the soil layer and the bedrock is distinctly resolved by a clear contrast in the resistivity values, with the soil layer missing between 35 m and 71 m along the profile, since this part of the profile is located on the forest road built directly on the bedrock. In the first 35 m of the profile, where existing, the soil layer reaches depths of just under 2 and up to about 7 m. A high resistivity anomaly ($\rho >$ 8000 Ωm) is resolved between meters 10 and 30, at a height between about 675 and 680 m. Both the anomaly position and the known location of the cave agree, thus, confirming our interpretation (Fig. 6b). A numerical modeling accounting for the position of the anomaly at this location also confirms that the geometry array can successfully solve for the cave (Fig. 6c).

The resistivity image of **P2** (Fig. 6d) also shows the boundary between the soil layer and the bedrock. The soil layer has a larger thickness (≈ 7 m) in the beginning and at the end of the profile, while in the middle it is narrower (≈ 2 m). Furthermore we resolve a distinct anomaly in the ERT image between meters 15 and 50 at a height between about 675 and 685 m. In contrast to **P1**, the interpretation of the field data and the outline of the Forststraß eneinbruch is not consistent (Fig. 6e). Especially between meters 20 and 40 there is a resistivity anomaly which is interpreted as a cavity based on the field data, but in fact there is no known cave part of the Forststraß eneinbruch. In the inversion of the synthetic data, derived from a model consisting of the known cave parts, the surrounding limestone and a soil layer on the surface, no anomaly is visible (Fig. 6f). Hence, in contrast to **P1**, the known positions of the cave chambers cannot explain the anomalies resolved in the ERT images of the field data.

The three parallel profiles (**P3**, **P4**, and **P5**) are above the eastern branch of the Forststraß eneinbruch, with **P3** crossing only the outermost edge of the cave. In the resistivity images (Fig. 6g, k, n), the boundary between the bedrock and the soil is resolved along all three profiles. The small thickness of the soil layer (< 1 m) resolved in the beginning of the profiles likely indicates the walls of a former quarry (displayed in Fig. 2a). Towards the end of the profiles, the soil layer reaches depths of up to 10 m. In all three profiles, two anomalies are resolved: The first at the beginning of the profiles (meters 0 to 10) with a lower resistivity (< 500 Ω*m*) than the surrounding rock. This anomaly is located at heights between 685 m and 690 m and reaches down to the resolution limit. A second anomaly, with higher resistivity (> 8000 Ω*m*), can be found between meters 20 and 35 at a height between 675 and 685 m. While this anomaly is clearly visible in the imaging results for **P3** and **P4** (Fig. 6g, k), it becomes smaller in **P5** (Fig. 6n). The position of the anomaly also changes from **P3** to P5. In **P3** it is from 25 to 35 m along the profile, in **P4** from 20 to 30 m and in **P5** from 20 to 25 m. In **P4** and **P5**, the position of the known cave chambers coincide well with the resistive anomaly (Fig. 6l, o). In **P5** the lower, mostly narrow cave-passages are not resolved in the ERT image. Also in **P3** the deep and narrow passages of the cave are not well resolved in the ERT image, since the resistive anomaly is above the known parts of the cave (Fig. 6h). Therefore, it seems unlikely that the clearly visible anomaly in the ERT image is produced just by these two narrow passages. For **P3**, the ERT image of the synthetic data (Fig. 6i) could not reproduce the anomaly visible in the ERT image of the field data, using just a model of the known cave parts (Fig. 6h). This is due to the limited spatial extension of the cave and

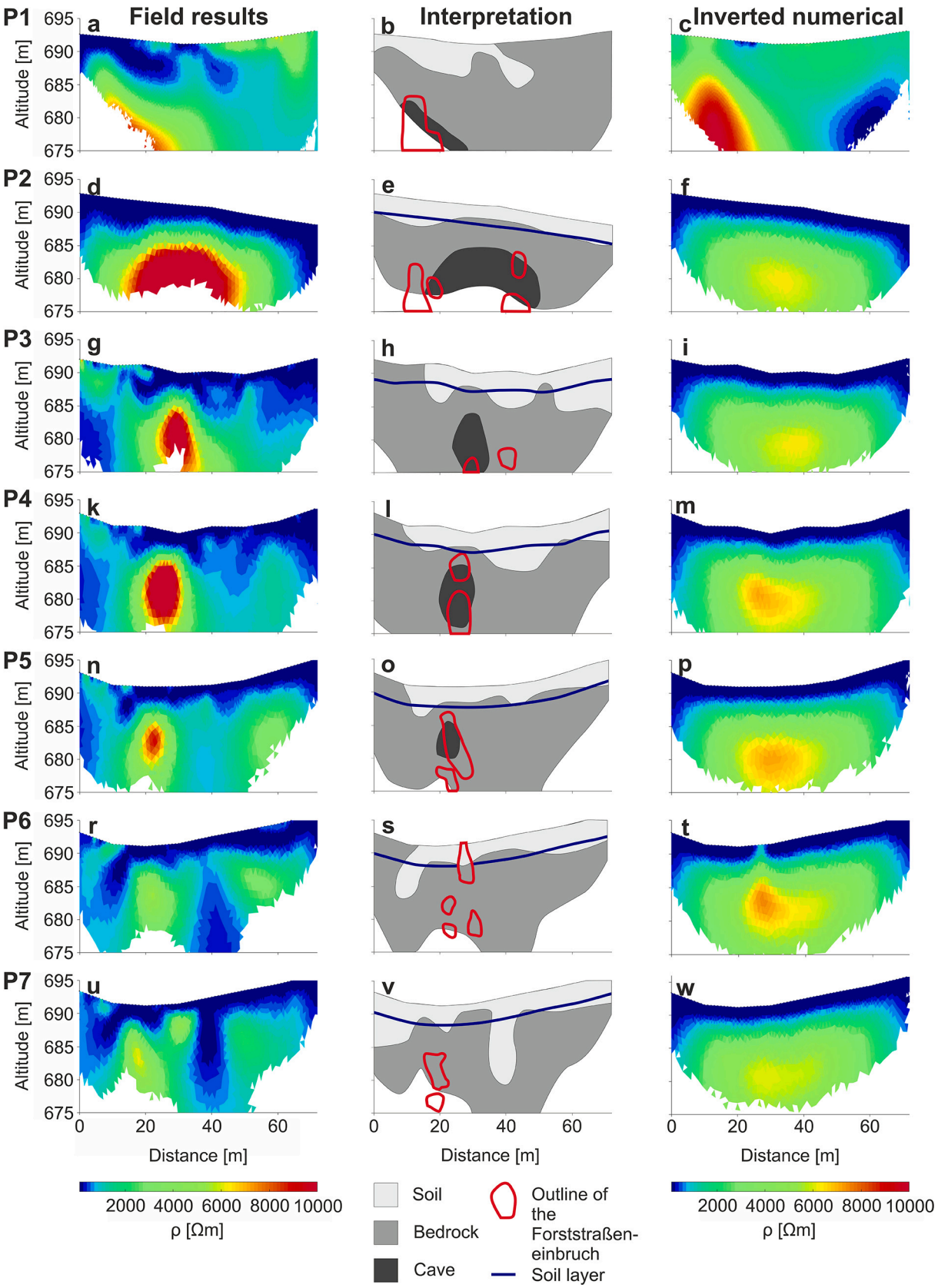

Fig. 6. Inversion images of the field data (first column), their interpretation (second column) and the inversion images of the synthetic data (third column) for all seven profiles (**P1–7**). In the second column, we give additional information about the underlying model (known outlines of the Forststraßeneinbruch and the used position of the soil layer).

its position at depths close to the resolution limit. The inversion images of the synthetic data of **P4** and **P5** (Fig. 6m, p) show a resistive anomaly, similar to that seen in the field data. In **P4**, the subsurface models obtained through inversion of the synthetic (Fig. 6m) and measured data (Fig. 6k) show good agreement, although the anomaly in the measured data is even more pronounced and reaches closer to the surface. An anomaly can also be seen in both the inversions of the measured (Fig. 6n) and synthetic data (Fig. 6p) of **P5**. However, its geometry and size differ between the measured and the synthetic data. The consistency between the synthetic and the field data reveal that to detect caves at a depth below 10 m, it is necessary to use a configuration with larger electrode separation which favors current injections at deeper positions and larger voltage dipoles to enhance higher signal to noise.

The profiles **P6** and **P7** are parallel to each other and to profiles **P3** to **P5**. They are located on both sides of the cave entrance and lie mainly above the deeper, western branch of the Forststraß eneinbruch. Both ERT images (Fig. 6r, u) show a similar behavior regarding the interface between soil and bedrock as well as the absence of any clear resistive anomaly. However, there are actually areas of the Forststraß eneinbruch below both profiles (Fig. 6s, v). The known cave parts below **P6** are visible according to the ERT images obtained for the synthetic data (Fig. 6t). In contrast to **P6**, the cave chambers below **P7** cannot be resolved in the inversion of the synthetic data (Fig. 6w). Hence, it can be concluded that the cave chamber below **P7** is too narrow, too deep and at least partially too close to the resolution limit to be visible in the ERT images.

3.2.1. Assess the differences identified in P2, P3, and P6

Profiles **P2** and **P3** clearly show resistive anomalies in the ERT images of the measured data (Fig. 6d, g), but none in the ERT images of the synthetic data (Fig. 6f, i), which leads to the assumption that there may be other still unknown cavities. The possible existence of uncharted cavities below **P2** and **P3** were investigated through the careful design of synthetic models, where we tested different depth and sizes of an additional cavity. Fig. 7 shows the field results (Fig. 7a, d), the models (Fig. 7b, e) and the inversion images of the synthetic data (Fig. 7c, f) for Profiles **P2** (upper row) and **P3** (lower row), which showed the best fit between the field and the synthetic data. For **P2** the inversion of the synthetic data (Fig. 7c) shows a large resistive anomaly, similar to that of the inversion of the field data (Fig. 7a). Therefore, the existence of at least one other cavity, inaccessible from the known cave, can be assumed. Also for **P3** the inversion of the adapted synthetic model (Fig. 7f) shows a resistive anomaly in the same region as the inversion of the field data (Fig. 7d). This suggests the presence of another cavity closer to the surface, although the imaging results for **P3** are not as clear as for **P2**.

In contrast to **P2** and **P3**, the ERT image of the measured data from **P6** show no anomaly (Fig. 6r), while one is visible in the ERT image of the synthetic data (Fig. 6t). From the investigations of the influence of soil or clay layers (Fig. 3k, l) we know that a layer of soil on the surface reduces the depth of investigation and negatively affects the detectability of a cavity. It has also been shown that a well conducting layer at the bottom of a cavity improves the determination of its geometry, especially the downward boundary (Fig. 3m). However, it is also possible that a layer of clay and sediment, not only on the bottom but also on the walls of a small cavity, completely masks it, as the current can easily flow around the cavity. This assumption could explain the absence of an anomaly, particularly in **P6**, where the near surface cavity extends into the sedimentary layer. It is known from the cave plan and cave exploration that the walls of the near-surface part of the cave are completely covered with sediment and clay. Based on these observations, a further model was constructed (Fig. 8b), which includes a highly conductive layer not only on the floor but also on the walls of the near-surface part of the cave. Fig. 8c shows the ERT image obtained by inversion of the corresponding synthetic data. As with the inversion of the field data (Fig. 8a), none of the cavities, even the deeper ones without sediments on the walls, are visible. This shows that a layer of clay and sediment on the cave walls in the surface-near region is sufficient to mask it and all parts of the cave below. The continuous, highly conductive layer of soil, similar to the one shown in the model **m2** (Fig. 3b), reduces the sensitivity at depth and prevents also detection of the deeper parts of the cave.

4. Conclusion

In the first part of this study, we investigated the reconstruction capabilities of the ERT for the investigation of caves associated with anomaly regions with high resistivity embedded in a karstic rock. For

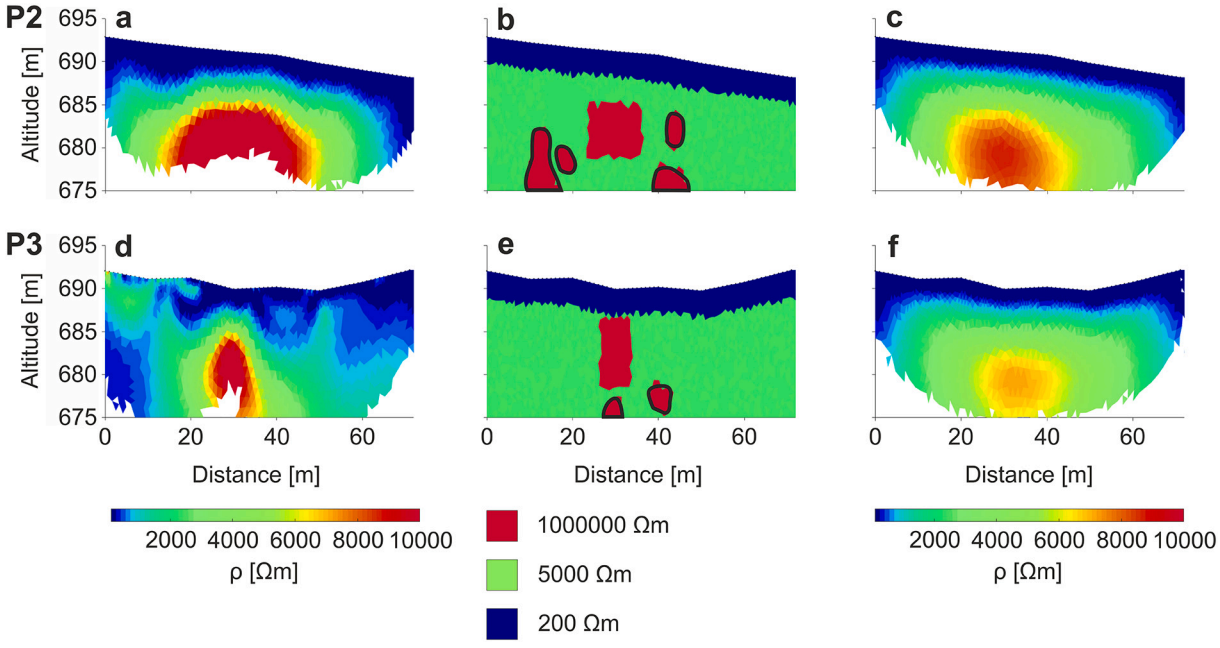

Fig. 7. ERT image after inversion of the field data (a, d), electrical model (b, e) of the subsurface below **P2** and **P3** and ERT image after inversion (c, f) with an additional cavity. The outlines of the Forststraßeneinbruch are shown as black lines.

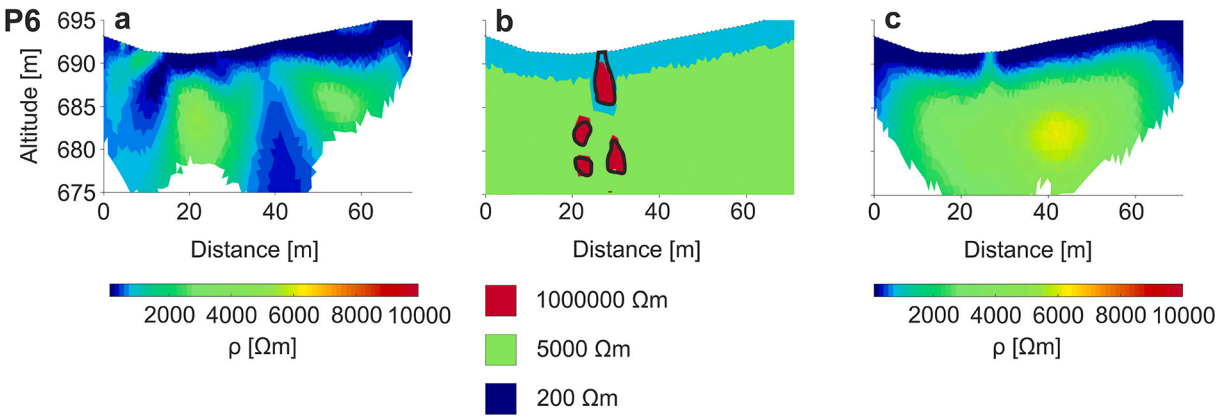

Fig. 8. ERT image after inversion of the field data (a), electrical model of the subsurface below P 6 (b) and ERT image after inversion (c) with a conductive layer on the cave walls of the near-surface cave parts. The outlines of the Forststraß eneinbruch are shown as black lines.

our analysis we defined different values in the resistivity of the karstic rocks, we also included conductive layers simulating soil on the top of the study area or accumulated at the bottom or walls of the caves. We want to investigate which contrasts in the electrical properties of karstic areas influence the ERT results. From these investigations we could show that (i) cavities can just be reconstructed when the surrounding rock has a high resistivity. (ii) A conductive soil layer reduces the depth of investigation. By analyzing the sensitivity, we were able to illustrate that here most of the current flows near the surface and does not reach the deeper areas. (iii) A more resistive top soil layer (200 Ωm) enhances the reconstruction of the cavity compared with a soil layer of 100 Ωm. (iv) A conductive soil layer at the bottom of a cavity improves the reconstruction of the cavity geometry, in particular the lower cavity boundary, while (v) a layer of clay and sediment not only on the bottom but also on the walls of a cavity may prevent its detection.

These fundamental investigations allowed us to enhance the interpretation of subsurface models obtained from field data collected in the vicinity of the Forststraß eneinbruch. By comparing the inversion images obtained for the measured and the synthetic data we could show, that the images for Profiles **P1**, **P4**, **P5**, **P6** and **P7** can be explained by the known cave chambers. The different geometry between the measured and synthetic data at **P4** and **P5** can be explained by the fact that the areas below these profiles are mostly narrow passages and the cave walls in this region are covered with sediment, which could decrease the resistivity due to electrolytic and surface conduction mechanisms. In two profiles (**P2** and **P3**), however, resistive anomalies occurred in the measurements that could not be explained by the known cavities. Therefore, further models were created that assume the existence of additional cavities that are neither accessible from the surface nor from the known parts of the cave. Based on these models, we assume the existence of additional cavities below **P2** and **P3**.

Caves are formed in water-soluble rock, such as limestone or dolomite, which generally has a high resistivity. Caves in wooded areas, which are also important for human infrastructure, are also likely to have a sedimentary floor in the parts of the cave close to the surface. The results of our study demonstrate that karst areas provide feasible conditions for the successful detection of cavities through the ERT method. However, with regard to the interpretation of the imaging results particular care has to be taken in presence of saturated conditions after rainfall events or during snowmelt. The same applies to highly conductive soil layers, which also occur mainly in wet conditions. Further investigations of the same area (cavity with sediment layer in the cave and on the surface above) with different levels of rock saturation could provide further information on which effect dominates under real conditions.

CRediT authorship contribution statement

Barbara Funk: Writing – original draft, Visualization, Software, Resources, Investigation, Formal analysis, Data curation, Conceptualization. **Adrian Flores-Orozco:** Writing – review & editing, Validation, Supervision, Software, Methodology, Funding acquisition, Conceptualization. **Matthias Steiner:** Writing – review & editing, Validation, Software, Methodology, Formal analysis.

Declaration of competing interest

The authors declare that they have no known competing financial interests or personal relationships that could have appeared to influence the work reported in this paper.

Data availability

Data will be made available on request.

Acknowledgments

BF thanks the support by the Austrian Science Fund (FWF): P36065-N. AFO and MS thank the support by the Austrian Science Fund (FWF): I6549-N. The authors thank the referees for there helpful suggestions.

Appendix A. Supplementary data

Supplementary data associated with this article can be found in the online version, at https://doi.org/10.1016/j.geomorph.2024.109332. These data include the Google map of the most important areas described in this article.

References

Amanatidou, E., Vargemezis, G., Tsourlos, P., 2022. Combined application of seismic and electrical geophysical methods for karst cavities detection: a case study at the campus of the new university of western macedonia, kozani, greece. J. Appl. Geophys. 196, 104499 https://doi.org/10.1016/j.jappgeo.2021.104499.

Archie, G., 1942. Fault rocks and fault mechanism. J. Geol. Soc. London 133, 191–213.

Artugyan, L., Ardelean, A.C., Urdea, P., 2020. GPR and ERT Investigations of Karst Structures at the Buhui-Cuptoare Cave System. Springer International Publishing, Cham, Anina Karst Region (Banat Mountains, Romania). https://doi.org/10.1007/978-3-030-28909-6-2.

Ba, X., Li, L., Wang, J., Zhang, W., Fang, Z., Sun, S., Liu, Z., Xiong, Y., 2020. Near-surface site investigation and imaging of karst cave using comprehensive geophysical and laser scanning: a case study in shandong, China. Environ. Earth Sci. 79, 298. https://doi.org/10.1007/s12665-020-09037-9.

Bauer, F., Ruttner, A., Schnabel, W., 1988. Geologische Karte der Republik Österreich - Blatt 71. Ybbsitz, Geologische Bundesanstalt.

Binley, A., Kemna, A., 2005. DC Resistivity and Induced Polarization Methods. Springer Netherlands, Dordrecht. https://doi.org/10.1007/1-4020-3102-5-5.

Carriére, S., Chalikakis, K., Sénéchal, G., Danquigny, C., Emblanch, C., 2013. Combining electrical resistivity tomography and ground penetrating radar to study geological structuring of karst unsaturated zone. J. Appl. Geophys. 94, 31–41. https://doi.org/10.1016/j.jappgeo.2013.03.014.

Chalikakis, K., Plagnes, V., Guerin, R., Valois, R., Bosch, F.P., 2011. Contribution of geophysical methods to karst-system exploration: an overview. Hydrgeol. J. 19, 1169–1180. https://doi.org/10.1007/s10040-011-0746-x.

Cheng, Q., Tao, M., Chen, X., Binley, A., 2019. Evaluation of electrical resistivity tomography (ert) for mapping the soil–rock interface in karstic environments. Environ. Earth Sci. 78, 439. https://doi.org/10.1007/s12665-019-8440-8.

De Waele, J., Gutiérrez, F., 2022. Karst Hydrogeology, Geomorphology and Caves. Wiley, Chichester. https://doi.org/10.1002/9781119605379.

Flores Orozco, A., Kemna, A., Zimmermann, E., 2012. Data error quantification in spectral induced polarization imaging. GEOPHYSICS 77, E227–E237. https://doi.org/10.1190/geo2010-0194.1.

Flores Orozco, A., Williams, K.H., Kemna, A., 2013. Time-lapse spectral induced polarization imaging of stimulated uranium bioremediation. Near Surf. Geophys. 11, 531–544. https://doi.org/10.3997/1873-0604.2013020.

Flores Orozco, A., Gallistl, J., Bücker, M., Williams, K., 2018. Decay curve analysis for data error quantification in time-domain induced polarization imaging. Geophysics 83, E75–E86. https://doi.org/10.1190/geo2016-0714.1.

Friedel, S., 2003. Resolution, stability and efficiency of resistivity tomography estimated from a generalized inverse approach. Geophys. J. Int. 153, 305–316. https://doi.org/10.1046/j.1365-246X.2003.01890.x.

Goldscheider, N., Chen, Z., Auler, A., Bakalowicz, M., Broda, S., Drew, D., Hartmann, J., Jiang, G., Moosdorf, N., Stevanovic, Z., Veni, G., 2020. Global distribution of carbonate rocks and karst water resources. Hydrgeol. J. 28, 1–17. https://doi.org/10.1007/s10040-020-02139-5.

Gómez-Ortiz, D., Martín-Crespo, T., 2012. Assessing the risk of subsidence of a sinkhole collapse using ground penetrating radar and electrical resistivity tomography. Eng. Geol. 149-150, 1–12. https://doi.org/10.1016/j.enggeo.2012.07.022.

Kemna, A., 2000. Tomographic Inversion of Complex Resistivity - Theory and Application. Ph.D. thesis.. Universität Bonn.

Kemna, A., Kulessa, B., Vereecken, H., Vanderborght, J., 2002. Imaging and characterisation of subsurface solute transport using electrical resistivity tomography (ERT) and equivalent transport models. J. Hydrol. 267, 125–146. https://doi.org/10.1016/S0022-1694(02)00145-2.

Khaldaoui, F., Djediat, Y., Baker, H., Ydri, A., Djeddi, M., Hamadou, K., Bouzar, A., 2020. Use of electrical resistivity tomography (ert) and electromagnetic induction (emi) methods to characterize karst hazards in north-eastern of algeria. Arab. J. Geosci. 13, 1204. https://doi.org/10.1007/s12517-020-06206-9.

LaBrecque, D., Daily, M., Ramirez, A., Owen, E., 1996. The effects of noise on occam's inversion of resistivity tomography data. Geophysics 61, 538–548. https://doi.org/10.1190/1.1443980.

Martel, R., Castellazzi, P., Gloaguen, E., Trépanier, L., Garfias, J., 2018. ERT, GPR, InSAR, and tracer tests to characterize karst aquifer systems under urban areas: the case of Quebec City. Geomorphology 310, 45–56. https://doi.org/10.1016/j.geomorph.2018.03.003.

Martínez-Moreno, F., Galindo-Zaldívar, J., Pedrera, A., Teixido, T., Ruano, P., Peña, J., González-Castillo, L., Ruiz-Constán, A., López-Chicano, M., Martín-Rosales, W., 2014. Integrated geophysical methods for studying the karst system of Gruta de las Maravillas (Aracena, Southwest Spain). J. Appl. Geophys. 107, 149–162. https://doi.org/10.1016/j.jappgeo.2014.05.021.

Moser, C., Binley, A., Flores Orozco, A., 2023. 3d electrode configurations for spectral induced polarization surveys of landfills. Waste Manag. 169, 208–222. https://doi.org/10.1016/j.wasman.2023.07.006.

Nguyen, F., Kemna, A., Antonsson, A., Engesgaard, P., Kuras, O., Ogilvy, R., Gisbert, J., Jorreto, S., Pulido-Bosch, A., 2009. Characterization of seawater intrusion using 2d electrical imaging. Near Surf. Geophys. 7, 377–390. https://doi.org/10.3997/1873-0604.2009025.

Niggli, P., 1948. Gesteine und Minerallagerstätten. Birkhäuser Basel. https://doi.org/10.1007/978-3-0348-7171-6.

Oldenburg, D.W., Li, Y., 1999. Estimating depth of investigation in dc resistivity and IP surveys. Geophysics 64, 403–416. https://doi.org/10.1190/1.1444545.

Park, K., Soliman, M., Je Kim, Y., Hyun Nam, B., 2024. Sinkhole stability chart for geotechnical investigation. Transp. Geotechnics 45, 101191. https://doi.org/10.1016/j.trgeo.2024.101191.

Pasierb, B., 2022. The application of the 2d/3d electrical resistivity tomography (ert) method in investigating the carbonate karst of the Zakrzówek horst. Geol. Geophys. Environ. 48, 319–327. https://doi.org/10.7494/geol.2022.48.3.319.

Puzzilli, L.M., Ruscito, V., Madonna, S., Gentili, F., Ruggiero, L., Ciotoli, G., Nisio, S., 2024. Natural sinkhole monitoring and characterization: the case of latera sinkhole (latium, Central Italy). Geosciences 14, 18. https://doi.org/10.3390/geosciences14010018.

Revil, A., Glover, P.W.J., 1998. Nature of surface electrical conductivity in natural sands, sandstones, and clays. Geophys. Res. Lett. 25, 691–694. https://doi.org/10.1029/98GL00296.

Spötl, C., Plan, L., Christian, E., 2016. Höhlen und Karst in Österreich. Oberösterreichisches Landesmuseum Linz, ISBN 9783854743217, p. 752.

Su, M., Liu, Y., Xue, Y., Cheng, K., Ning, Z., Li, G., Zhang, K., 2021. Detection method of karst features around tunnel construction by multi-resistivity data-fusion pseudo-3d-imaging based on the pca approach. Eng. Geol. 288, 106127 https://doi.org/10.1016/j.enggeo.2021.106127.

Tao, M., Cheng, X.C.Q., Binley, A., 2022. Evaluating the joint use of gpr and ert on mapping shallow subsurface features of karst critical zone in Southwest China. Vadose Zone J. 21, e20172 https://doi.org/10.1002/vzj2.20172.

Valois, R., Camerlynck, C., Dhemaied, A., Guerin, R., Hovhannissian, G., Plagnes, V., Rejiba, F., Robain, H., 2011. Assessment of doline geometry using geophysics on the Quercy plateau karst (South France). Earth Surf. Process. Landf. 36, 1183–1192. https://doi.org/10.1002/esp.2144.

Verdet, C., Sirieix, C., Marache, A., Riss, J., Portais, J.C., 2020. Detection of undercover karst features by geophysics (ert) lascaux cave hill. Geomorphology 360, 107177. https://doi.org/10.1016/j.geomorph.2020.107177.

Waxman, M., Smits, L., 1968. Electrical conductivities in oil-bearing shaly sands. Soc. Pet. Eng. J. 8, 107–122. https://doi.org/10.2118/1863-A.

Weigand, M., Flores Orozco, A., Kemna, A., 2017. Reconstruction quality of sip parameters in multi-frequency complex resistivity imaging. Near Surf. Geophys. 15, 187–199. https://doi.org/10.3997/1873-0604.2016050.

Yue, Y., Guo, Z., Luo, W., Zhang, G., Chen, N., 2020. Combination of ert and em methods in the exploration of karst caves and foundation in the nujiang airport survey of China. IOP Conf. Ser. Earth Environ. Sci. 569, 12–16. https://doi.org/10.1088/1755-1315/569/1/012016.

Zhang, J., Liu, S., Chen, Q., Wang, B., Ren, C., 2019. Application of cross-borehole integrated geophysical methods for the detailed investigation of karst in urban metro construction. J. Environ. Eng. Geophys. 24, 525–536. https://doi.org/10.2113/JEEG24.04.03.525.